Catalysis Today 154 (2010) 142–148

Contents lists available at ScienceDirect

Catalysis Today

journal homepage: www.elsevier.com/locate/cattod

Iron oxide nanoparticles on flat oxidic surfaces—Introducing a new model catalyst for Fischer–Tropsch catalysis

P. Moodley[a,b], F.J.E. Scheijen[a], J.W. Niemantsverdriet[a], P.C. Thüne[a,*]

[a] Schuit Institute of Catalysis, Eindhoven University of Technology, P.O. Box 513, 5600 MB Eindhoven, The Netherlands
[b] Sasol Technology, P.O. Box 1, Sasolburg 1947, South Africa

ARTICLE INFO

Article history:
Available online 24 April 2010

We would like to dedicate this work to Ben Nieuwenhuys, our esteemed colleague and pleasant room partner in Eindhoven.

Keywords:
Iron oxide
Model catalyst
Nanoparticles
Transmission electron microscopy (TEM)
X-ray photoelectron spectroscopy (XPS)
Fischer–Tropsch catalysis

ABSTRACT

Spincoating colloidal solutions of monodisperse nanoparticles onto flat silica supports offers a facile and flexible way to produce model catalysts with well defined catalyst loading and particle size. By spincoating iron oxide (magnetite) nanoparticles with varying particle diameter we produce a model system for iron based Fischer–Tropsch catalysts. In this proof of principle study we employ a combination of surface spectroscopy (XPS) and transmission electron microscopy (TEM) to investigate the changes in surface chemistry and morphology of the model catalysts upon catalyst pretreatment and exposure to syngas.

1. Introduction

Surface science models featuring catalytic nanoparticles on flat oxidic supports have proven to be a powerful approach to probe the surface chemistry and the nanoscale material science of catalysts [1–7]. Such model catalysts are typically prepared by vacuum based techniques as chemical vapor deposition [8,9] or e-beam lithography [10,11]. Preparation routes via the liquid phase, which are inherently closer to preparation routes for high surface area catalysts usually involve spincoating catalyst precursors typically from aqueous solutions [12–15].

Iron oxide nanoparticles are attractive materials in a number of research and industrial fields such as magnetic storage media [16,17], drug delivery [18–23] and gas sensing [24–26]. Iron oxide nanoparticles are active catalysts in CO and methane oxidation [27–29], or serve as cocatalyst in the extremely active Au/FeO_x catalyst for selective CO oxidation [30–32]. Metallic iron nanoparticles size-selectively produce carbon nanotubes in catalytic CVD [33–38].

Over the past years a number of reliable and elegant preparation routes towards size-selective iron oxide nanoparticles from nontoxic precursors have been described in literature [39–43]. Iron oxide nanoparticles form stable colloidal solutions that can be handled in air and are conveniently dispersed on flat substrates by spincoating impregnation. Therefore these nanoparticles form ideal precursors for morphological studies in catalyst preparation, activation and deactivation. Using Iron oxide nanoparticles as an example in the following we want to illustrate how the combination of colloidal nanoparticles with electron transparent silica supports forms a versatile platform to study morphological changes in catalyst preparation, activation and deactivation. We will particular look at the changes in surface chemistry and morphology of the silica supported iron oxide nanoparticles during calcination (20% O_2 in Ar at 500 °C) and subsequent reduction in H_2, CO and CO/H_2.

2. Experimental

2.1. SiO_2/SiN_x TEM grids

The silica TEM substrates used for our research were custom made according to requested specifications. The side view of a typical TEM substrate is shown in Fig. 1. The basic preparation involved the deposition of silicon nitride both at the back and front of a standard silicon (1 0 0) wafer. The nitride at the back was patterned to form an appropriate mask which facilitated anisotropic etching of the silicon, until the silicon nitride at the top was left suspended in its framework. The silicon nitride layer on the top was made as

* Corresponding author. Tel.: +31 40 2474997; fax: +31 40 247 3481.
E-mail address: p.c.thuene@tue.nl (P.C. Thüne).

0920-5861/$ – see front matter © 2010 Elsevier B.V. All rights reserved.
doi:10.1016/j.cattod.2010.03.020

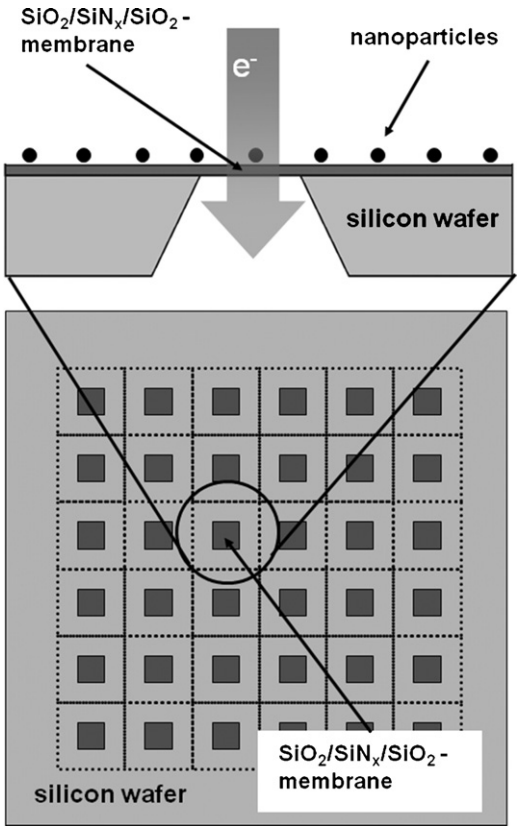

Fig. 1. (top) Schematic cross section through a silica TEM grid. The 200 μm × 200 μm electron transparent membrane consist of a 15 nm thick silicon nitride film, which is oxidized at 750 °C to produce a 3 nm thick silicon dioxide surface layer. (bottom) Schematic top view of a 6 × 6 array of fused TEM grids stabilized by a 2 mm wide silicon frame.

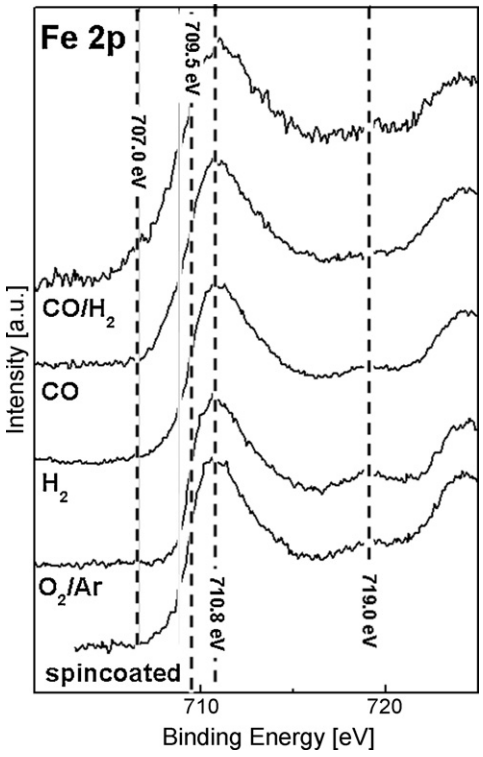

Fig. 2. Fe $2p_{3/2}$ window spectra of 9 nm FeO_x/SiO_2 model catalysts at different stages of catalyst preparation. Spincoated denotes model catalyst after spincoating impregnation; O_2/Ar denotes catalyst after calcination at 500 °C in 20% O_2/Ar; H_2, CO and H_2/CO denote subsequent reduction at 320 °C for 18 h in the respective gas mixtures. The dashed vertical lines indicate metallic iron (707.0 eV), Fe^{2+} in Fe_3O_4, (709.5 eV), Fe^{3+} in γ-Fe_2O_3 of Fe_3O_4 (710.8 eV) and the Fe^{3+}-satellite (719.0 eV).

thin as possible (±15 nm) to facilitate efficient TEM analysis. A silica surface layer of about 3 nm thickness was formed by calcining the wafer in air at 750 °C for 24 h. The silica TEM grid used for our model catalysts were made to have a window with dimensions of 200 μm × 200 μm to allow for stability and adequate TEM imaging area. In order to allow spincoating impregnation 36 TEM grids were arranged in a square and stabilized by a silicon frame. The fused silica TEM grids are robust and survive spin coating up to 2800 rpm as well as high reaction temperatures and gas flows to capture the top view of the catalyst in its pristine state.

2.2. Synthesis of the FeO_x/SiO_2 model catalysts

The iron oxide nanoparticles used in this study were prepared by thermal; decomposition of iron(III)oleate complexes in high boiling solvents. The 9.5 nm and 16 nm iron oxide nanoparticles were obtained in refluxing 1-hexadecene and 1-octadecene respectively as described by Park et al. [39]. 28 nm iron oxide nanoparticles were prepared as described by Yu et al. [40]. 2 mmol iron oxide hydrate and 16 mmol of oleic acid were heated to 320 °C in 6.5 ml of 1 octadecene for 2 h. This method is essentially a variation of the previous as here the iron oleate complex is formed in situ during the heating of the reaction mixture.

Solutions of the iron nanoparticles in toluene were sonicated using a horn sonicator (SonicVibracell VC750) with a cylindrical tip (6 mm end cap diameter) delivering about 3000 J/min. The sonicated solutions were then spincoated on flat silica supports, which were either calcined silicon nitride TEM grids or silicon wafers with a 20 nm thick layer of thermal silicon dioxide.

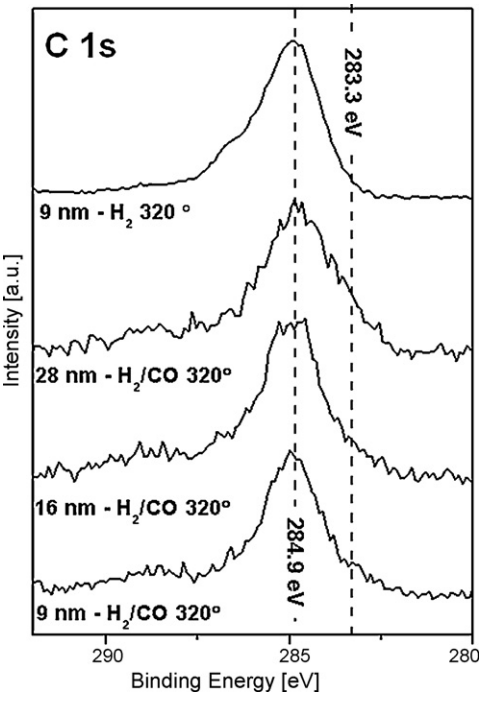

Fig. 3. C 1s window spectra of precalcined catalysts after reduction in H_2 or H_2/CO. The vertical lines indicate hydrocarbon impurities (284.9 eV) and carbidic carbon (283.3 eV).

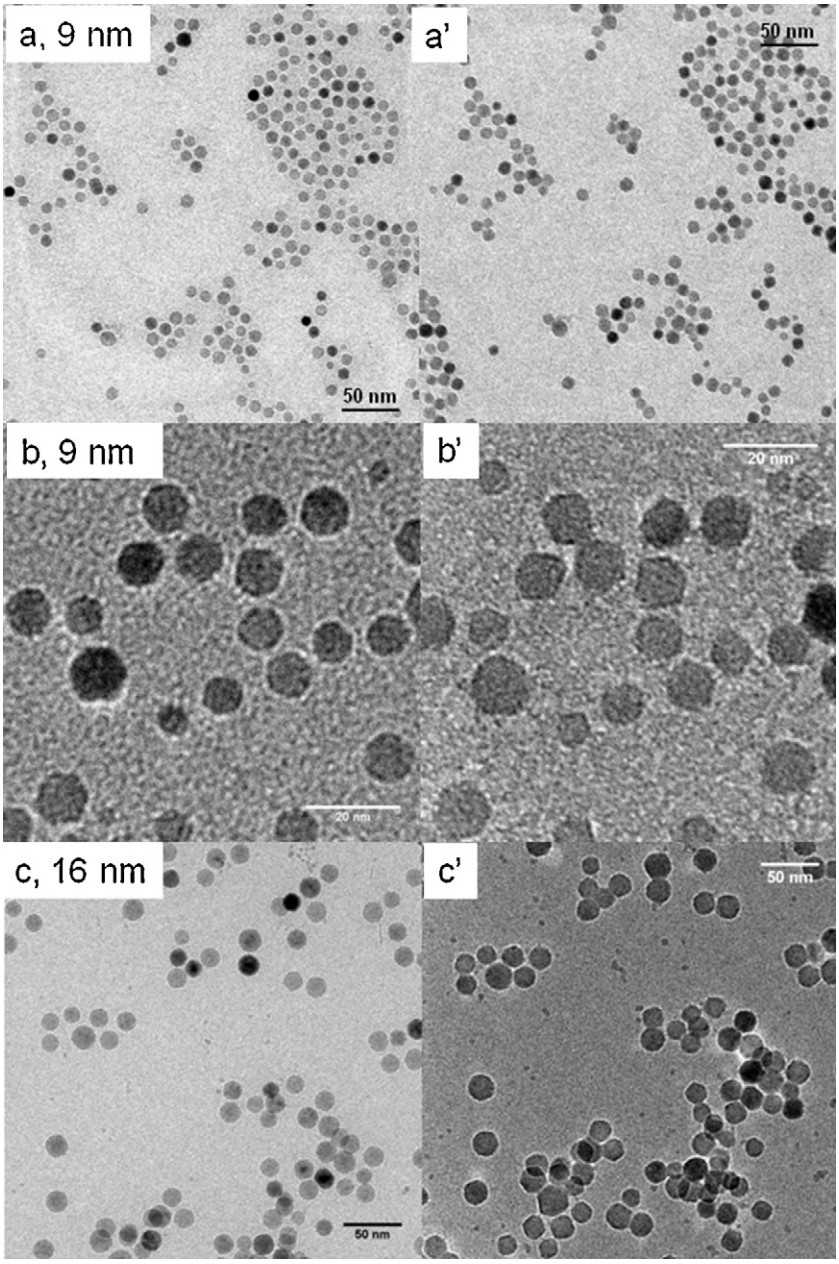

Fig. 4. TEM micrographs of 9 nm (a and b) and 16 nm (c) magnetite nanoparticles dispersed on a SiO_2/SiN_x membrane after spincoating impregnation (left column) and after calcination (a′–c′, right column).

All gas treatments were performed inside a quarts tube reactor in flowing gas stream (±100 ml/min) at atmospheric pressure. H_2 (5.0), CO (4.7) and 20% O_2/Ar (5.0) were purchased from Linde and purified with Cu/Al_2O_3 and molecular sieves.

3. Materials

Iron(III) choride hexahydrate (97%), sodium oleate (99%), 1-hexadecene (92%), oleic acid (90%), toluene (99.5%) and hydrated iron oxide hydrate (50–80 mesh) were purchased from Aldrich, 1-octadecene (>95%) was purchased from Fluka. All chemicals and solvents were used as received.

3.1. Analysis

XPS was measured with a Kratos AXIS Ultra spectrometer, equipped with a monochromatic Al Kα X-ray source and a delay-line detector (DLD). Spectra were obtained using the aluminum anode (Al Kα = 1486.6 eV) operating at 150 W. Spectra were recorded at background pressure, 2×10^{-9} mbar. Binding energies were calibrated to Si 2p peak of amorphous silica at 103.3 eV. The TEM studies were carried out on a Tecnai 20 (FEI Co.) operated at 200 kV.

4. Results

Iron oxide particles prepared from iron(III) oleate complexes consist of mixtures of γ-Fe_2O_3 and Fe_3O_4. Increasing the particle diameter results in an increased magnetite contribution [39]. These particles are stabilized in solution by the oleate surfactants. After spincoating impregnation onto $SiO_2/Si(1\,0\,0)$ model supports the surfactants are removed by calcination in dry O_2/Ar at 500 °C and atmospheric pressure. Subsequently the model catalysts are treated with H_2, CO and CO/H_2 (1/1) at 320 °C for 18 h the XPS

spectra shown in Fig. 2 show the evolution of the Fe $2p_{3/2}$ region of 9 nm particles upon these treatments. Fe_3O_4 and γ-Fe_2O_3 have very similar Fe 2p signals with a peak maximum at 710.8 eV. The iron oxide phases phase can best be distinguished on the basis of their peak shape [44,45]. While magnetite shows a low binding energy shoulder at about 709.5 eV due to the presence of Fe^{2+} ions (in an oxide matrix), γ-Fe_2O_3 features a characteristic Fe^{3+} satellite peak at about 719.0 eV. Upon calcination, the satellite peak becomes more pronounced while the low binding energy shoulder diminishes. This observation is in line with the expected oxidation towards a pure γ-Fe_2O_3. Reduction with hydrogen induces only minor changes the Fe $2p_{3/2}$ emission implying that the 9 nm iron oxide nanoparticles are not reduced under these conditions. Treatment with CO results in the disappearance of the Fe^{3+} satellite peak. While the Fe $2p_{3/2}$ peak maximum remains at 710.8 eV, we observe the evolution of a pronounced low binding energy shoulder with an inversion point at 709.5 eV. These observations point towards reduction to Fe_3O_4 while we find no evidence for the formation of iron carbides or metallic iron. However, upon subsequent treatment in CO/H_2 we observe a low binding energy shoulder at 707.0 eV while the peak maximum remains at 710.8 eV. The low binding energy shoulder indicates that that at least some of the iron has been reduced to the metallic state ($Fe^{(0)}$: 706.8 eV) or to iron carbides. Butt reported 707.3 eV for χ-Fe_5C_2 in Ref. [46] while Bonnet et al. report 708.1 eV in Ref. [47]. Note that we have corrected the values from Bonnet et al. by −0.4 eV to place the aliphatic hydrocarbon component at 285.0 eV thus matching our energy calibration. The main component of the Fe $2p_{3/2}$ remains at about 710.8 eV. It is difficult to judge the degree of reduction of the iron nanoparticles by XPS due to partial reoxidation after sample transfer through a glovebox. However, TEM analysis will reveal that the 9 nm iron oxide nanoparticles remained largely crystalline Fe_3O_4.

The C 1s window spectra in Fig. 3 support the formation of iron carbide species after treatment with CO/H_2. We observe a strong contribution at 283.3 eV, which is quite comparable to the values found by Butt [46] (χ-Fe_5C_2 283.2 eV) or by Bonnet et al. [47] (283.4 eV). This contribution becomes more prominent for larger particles. We assign the contribution at 284.9 eV to hydrocarbon impurities that inevitably adsorb on the model catalysts during sample transfer through the glovebox ambient.

Iron oxide nanoparticles were dispersed onto the fused silica TEM grids by spincoating impregnation to allow a detailed analysis on the effect of catalyst pretreatments on the particle morphology. The nanoparticles seem to have a tendency to agglomerate on the silica surface to form small two-dimensional islands. However, on a typical model catalyst isolated particles coexist with particle pairs, small two-dimensional clusters consisting of a few nanoparticles or even extended, randomly shaped two-dimensional islands. Because of the oleic acid surfactant the individual iron oxide nanoparticles remain separated on the silica surface by at least 2.2 nm. In this fashion the iron oxide nanoparticles arrange into "constellations" that can be conveniently used to navigate on the SiO_2/SiN_x membrane and to revisit individual nanoparticles after chemical treatments.

In Fig. 4 we present such constellations of supported 9 nm (Fig. 4a and b) and 16 nm (Fig. 4c) nanoparticles to observe the effect of calcination in dry air (O_2/Ar 20/80) on these particles. The left column (Fig. 4a–c) shows the particles after impregnation, the right column (Fig. 4a′–c′) shows the same set of particles after calcination. For both particle sizes we find that calcination has subtle but distinct effects on the morphology of model catalysts. The particles projections remain largely circular even though the particle faceting is a bit more visible after calcination. The particle diameters, increase significantly. The diameters of the 9 nm particles increases in average only by 0.5 nm while 16 nm iron oxide nanoparticles show an 4 nm increase in diameter upon calcination.

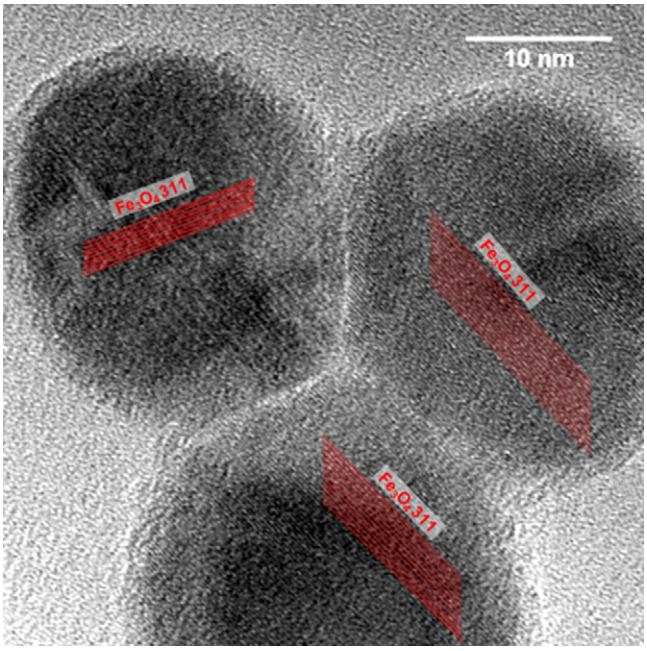

Fig. 5. High resolution TEM images of 28 nm FeO_x-nanoparticles after calcination.

As we observe no examples for particles with decreasing diameter after calcination we can rule out Ostwald ripening as the cause of this behavior. Also the oxidation from Fe_3O_4 to γ-Fe_2O_3 cannot explain the increase in diameter as they belong to the same space group (*Fd*3*m*) and their lattice parameters differ by less than 1% [48]. Instead we attribute this observation to a bonding interaction between the iron oxide nanoparticles and the silica substrate that causes the nanoparticles to flatten. The relative distances between the center of mass of the iron oxide nanoparticles after calcination remain constant within the 0.2 nm with respect to the same particles before calcination. This corresponds to the accuracy of the distance measurements. Note however that there is one exception: 9 nm particles in close proximity (below 1.5 nm) often touch each other after calcination while the centers of mass have moved typically by 1 nm towards each other. On the other hand there are also examples of close neighbors which remain immobile and remain separated after calcination. The 16 nm particles spread out much more than the 9 nm particles, therefore close neighbors are much more likely to fuse together during calcination. The fusion of iron oxide nanoparticles is linked to the surface wetting on the silica substrate. As this causes a larger expansion of the particle footprint for larger iron oxide particles, these particles are more prone to coalescence.

Fig. 5 shows three 28 nm iron oxide particles which are fused together after calcination. The original single crystalline particles remain clearly discernable and they become connected by amorphous grain boundaries.

As we have seen in the XPS analysis of the 9 nm particles it seems to be difficult to reduce iron oxide nanoparticles. Reduction in CO gave only a minimal reduction to Fe_3O_4. Only after a 18 h treatment in CO/H_2 at 320 °C we observed a relatively small contribution from metallic iron while the main contribution still comes from oxidic iron. In Fig. 6 we observe the effect of reduction of iron oxide nanoparticles with different sizes with CO/H_2 1/1. The left column shows silica supported nanoparticles with 9 nm (Fig. 6a), 16 nm (Fig. 6b) and 28 nm (Fig. 6c) after calcination. The right column (Fig. 6a′–c′) shows the same particles after treatment with CO/H_2 1/1. We observe for all particle sizes the development of core shell structures, which become more pronounced for larger particle sizes.

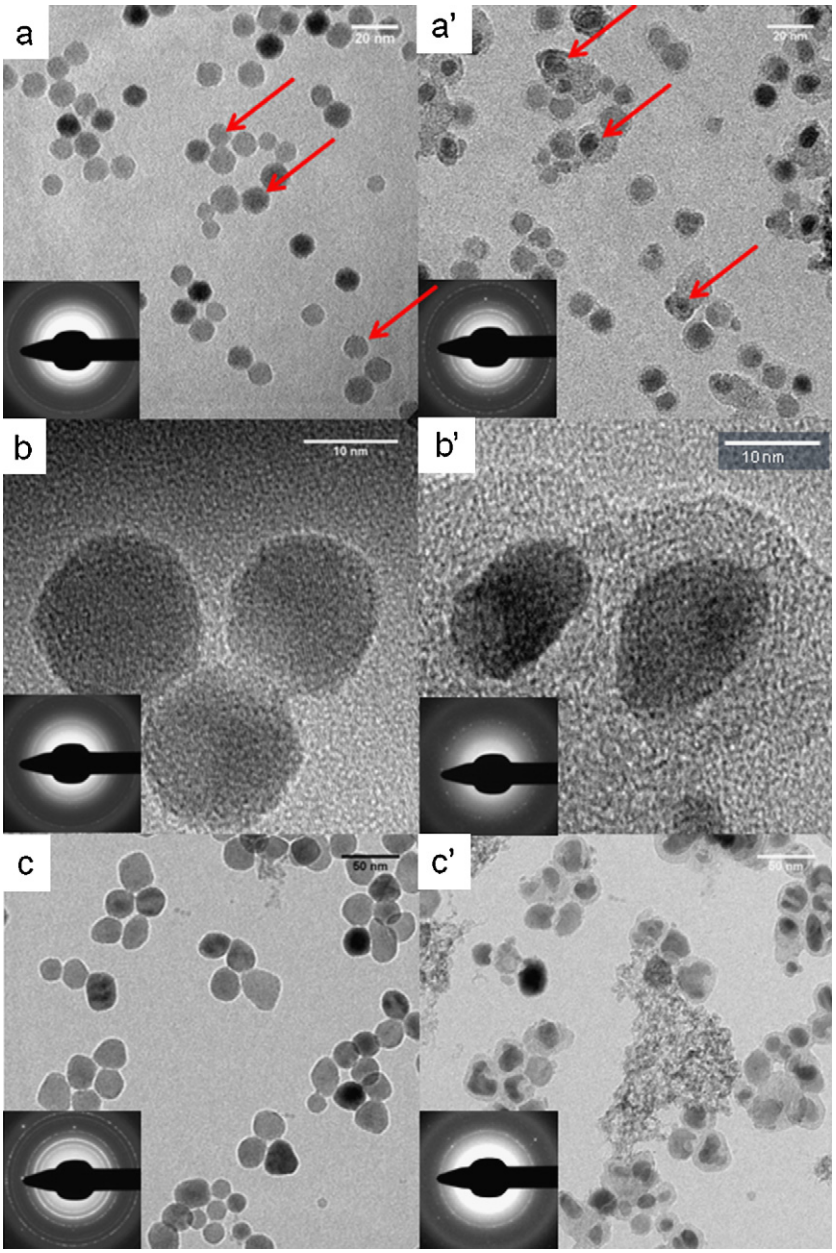

Fig. 6. TEM micrographs of 9 nm (a), 16 nm (b) and 28 nm (c) particles dispersed on a SiO_2/SiN_x membrane after calcination in 20% O_2/Ar at 320 °C (left column) and after reduction in CO/H_2 1/1at 320 °C (a′–c′, right column). The insets in the bottom left corners of the images show the corresponding electron diffractograms.

All samples show the typical electron diffraction patterns for Fe_3O_4 or γ-Fe_2O_3 after calcination. After syngas treatment the 9 nm particles show basically the same diffraction pattern. This implies that the oxide particles remain largely intact during the syngas treatment, even though some particles indicated by the arrows were probably transformed into iron carbide. Note that a small extent of reduction was also evident from the XPS spectra (Fig. 2). However, for the larger particles we observe a somewhat diffuse diffraction ring at about $0.21 \pm 0.01\ nm^{-1}$ typical for iron carbides according to Datye and coworkers [49,50]. The diffractions of iron oxides have become indiscernible implying that in contrast to the 9 nm particles the 16 nm and the 28 nm are converted almost quantitatively to iron carbides.

After reduction in syngas we observe an additional amorphous phase that is distributed in irregular patches on the model catalyst (see Fig. 6c′). The nature of this phase remains ambiguous as we have no possibility to analyze these features, e.g. by means of EELS. We tentatively assign this phase as amorphous carbon of yet unknown origin.

In the high resolution images in Fig. 7 we observe one particular 28 nm particle, revealing lattice fringes after calcination and after CO/H_2 treatment. It appears that the single crystalline γ-Fe_2O_3 particle, which was covered with a 1 nm thick amorphous oxide shell was transformed into a crystalline carbide particle with a lattice spacing of 0.22 nm.

The syngas reduced 28 nm particles shown in Fig. 6c′ and in Fig. 7 are of striking resemblance to the CO carburized catalyst presented in Ref. [49] The lattice fringes of the crystalline carbide cores are the same. Also the surrounding shells look very similar, they appear amorphous with a slight tendency towards a layered structure. We find an interlayer distance of approximately 0.34 nm, which is good agreement with the expected 0.335 nm found in graphite.

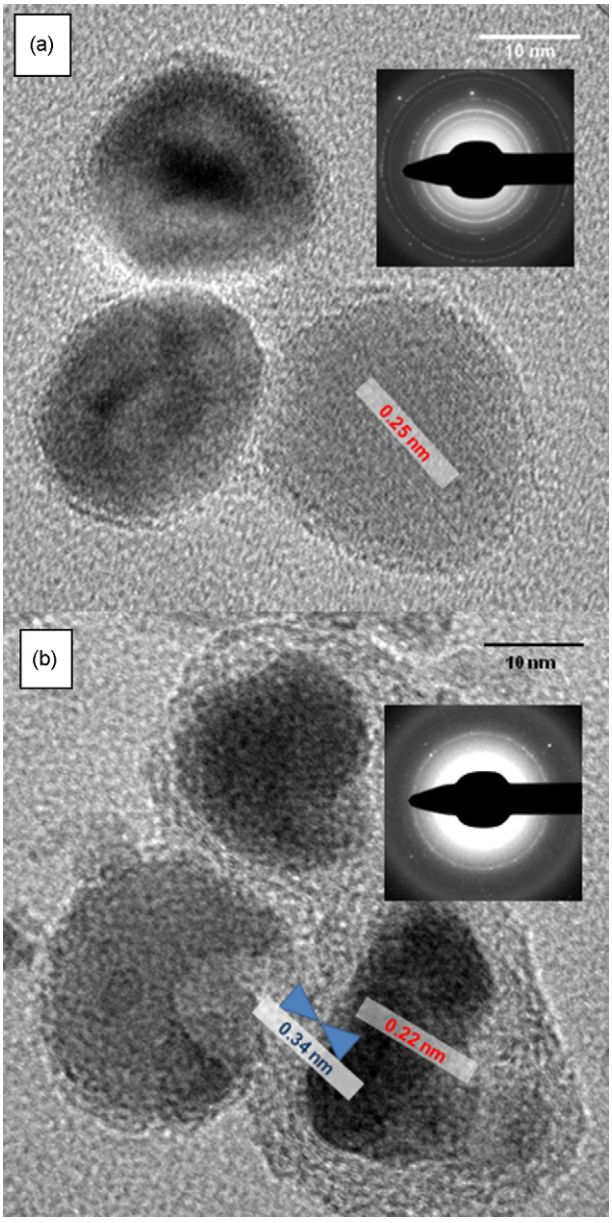

Fig. 7. High resolution images of 28 nm FeO_x-nanoparticles after calcination in 20% O_2/Ar at 500 °C, and after reduction in H_2/CO 1/1. Insets show corresponding electron diffractograms.

5. Discussion

When magnetite nanoparticles with 9, 16 and 28 nm diameter are dispersed onto flat silica supports by spincoating impregnation from colloidal solutions the particles arrange randomly on the support with a slight tendency for small two-dimensional islands. The individual particles are separated by at least 2.2 nm due to steric repulsion of the surfactants. Upon calcination the particles are oxidized to γ-Fe_2O_3. We observe that calcination causes the removal of the organic surfactant and the anchoring of the iron oxide nanoparticles onto the flat silica surface at their original point of deposition, the iron oxide wets the silica surface causing the particles to spread somewhat on the silica support. This is an indirect indication for the formation of iron silicates at the iron oxide-silica interface. For the 16 and 28 nm particles the increase in projected diameter is so large that individual particles fuse together forming amorphous grain boundaries between the individual crystals. We find no evidence for sintering by Ostwald ripening during calcination. The magnetite nanoparticles are difficult to reduce. Treatment of the calcined nanoparticles with pure hydrogen and pure carbon monoxide at 320 °C has only a very minor effect on the surface chemistry and morphololgy. The γ-Fe_2O_3 particles are merely reduced back to Fe_3O_4.

The 9 nm magnetite particles remain largely inert also against reduction in H_2/CO 1/1 at 320 °C. While XPS reveals a small contribution of reduced iron (metal or carbide) TEM and electron diffraction indicate that the main component remains crystalline magnetite. Apparently silica supported magnetite is very difficult to reduce. However apart from the interfacial iron silicate formed during calcination we find no indication for formation of additional silicate on the surface of the magnetite particles.

As Datye and coworkers have shown in Ref. [50] magnetite evolves from bulk α-Fe_2O_3 during pre-reduction and forms a "support" on which iron carbides are slowly formed during Fischer–Tropsch synthesis. Bukur et al. [51] and Wu et al. [52] have demonstrated that for mixed α-Fe_2O_3/Fe_3O_4 catalysts the degree of carburization during syngas treatment decreases with increasing magnetite content. Formation of iron silicates is not to be expected as these are formed from silica supported α-Fe_2O_3 and FeOOH during activation with hydrogen or syngas [53,54]. In fact formation of iron carbides from magnetite might not be expected at all as the reverse reaction is observed under Fischer–Tropsch conditions. In a recent study combining in situ X-ray adsorption spectroscopy and wide angle X-ray scattering de Smit et al. [55] have investigated the structural changes of a Fe_2O_3–Cu–K–Si catalyst during pretreatments and during Fischer–Tropsch synthesis. Activation with CO/H_2 at 450 °C resulted in the formation of 12 nm metallic iron particles which were partially converted into χ-Fe_5C_2 during subsequent Fischer–Tropsch synthesis. However, pretreatment with hydrogen at 350 °C resulted in catalyst containing mainly Fe_3O_4 and Fe_2SiO_4 which remained stable under Fischer–Tropsch conditions The hydrogen reduced catalyst in Ref. [55] behaves similar to our silicon supported 9 nm magnetite nanoparticles. However, the 16 nm and 28 nm particles in our study are almost quantitatively converted into iron carbides that are encapsulated in graphitic carbon. The reason for this reactivity lies probably in the extreme dry conditions of our syngas treatment, which is a consequence of the low conversion due to the small amount of iron on our flat model supports. The reason for the low reducability of the 9 nm particles is not quite clear. As we see no evidence for encapsulation in iron silicate we do not believe that iron–silica interactions are responsible for this behavior. Possibly the reducibility of the magnetite particles is related to their surface crystallinity. It appears that the 16 nm and the 28 nm particles feature a thin film of amorphous iron oxide after calcination. This surface layer should be reduced relatively easily under Fischer–Tropsch conditions and serve as a catalyst for the reduction of the crystalline core. The 9 nm particles seem to have a higher crystallinity at the surface making them more difficult to reduce.

6. Conclusions

In this proof of principle study we have introduced a new type of model catalyst, which is made from spincoating colloidal suspensions of catalyst nanoparticles onto a flat oxidic support. As an example we have dispersed iron oxide nanoparticles onto flat silica supports aiming at modeling iron based Fischer–Tropsch catalysts. We have followed the changes in morphology and surface chemistry of the model catalysts after different catalyst pretreatments including calcination and reduction in hydrogen, carbon monoxide and a 1/1 mixture of carbon monoxide and hydrogen.

Next to a conventional surface analysis with photoelectron spectroscopy we were able to investigate the morphology of the model catalyst with transmission electron spectroscopy using newly developed fused silica TEM grids.

We present here our initial data to demonstrate the potential of the new approach rather than to give a detailed analysis on the surface chemistry and morphology of silica promoted iron based Fischer–Tropsch.

In an assessment of the new approach we want to make the following points:

- Spincoating colloidal solution of catalyst nanoparticles instead of conventional precursor salts onto flat oxide support allows a simultaneous control of catalyst loading and particle size.
- The fused silica TEM grids are very robust model supports that allow spincoating and thermal treatment under harsh conditions.
- The magnetite nanoparticles used in this study become firmly anchored onto the silica surface upon calcination, probably due to formation of iron silicate interface layer.
- Reduction of the silica supported magnetite nanoparticles in hydrogen of carbon monoxide is difficult, however in mixed hydrogen/carbon monoxide atmosphere and under the strict absence of water they are transformed directly into iron carbides. This reduction does not seem to proceed via iron silicate intermediates.

In summary iron oxide nanoparticles supported on flat silica surfaces and thin, electron beam transparent silica membranes form a promising new model system for iron based Fischer–Tropsch catalysts. In the near future we plan to extend this approach towards other iron oxide phases and towards the incorporation of promotors into the iron oxide nanoparticles.

References

[1] C.T. Campbell, Surf. Sci. Rep. 27 (1997) 1.
[2] P.L.J. Gunter, J.W. Niemantsverdriet, F.H. Ribeiro, G.A. Somorjai, Catal. Rev. 39 (1997) 77.
[3] C.R. Henry, Surf. Sci. Rep. 31 (1998) 235–325.
[4] R. Schlögl, S.B. Abd Hamid, Angew. Chem. Int. Ed. 43 (2004) 1628.
[5] M. Bowker, Surf. Sci. 603 (2009) 2359.
[6] A.P. Seitsonen, H. Over, Surf. Sci. 603 (2009) 1717–1723.
[7] P.C. Thüne, J.W. Niemantsverdriet, Surf. Sci. 603 (2009) 1756–1762.
[8] D.W. Goodman, J. Catal. 216 (2003) 213.
[9] S.M. McClure, M. Lundwall, F. Yang, Z. Zhou, D.W. Goodman, J. Phys. Chem. C 113 (2009) 9688.
[10] G.A. Somorjai, R.M. Rioux, Catal. Today 100 (2005) 201.
[11] G.A. Somorjai, Appl. Surf. Sci. 121 (1997) 1.
[12] E.W. Kuipers, C. Laszlo, W. Wieldraaijer, Catal. Lett. 17 (1993) 71.
[13] R.M. van Hardeveld, P.L.J. Gunter, L.J. van IJzendoorn, W. Wieldraaijer, E.W. Kuipers, J.W. Niemantsverdriet, Appl. Surf. Sci. 84 (1995) 339.
[14] M.A. Brookshier, C.C. Chusuei, D.W. Goodman, Langmuir 15 (1999) 2043.
[15] J.W. Niemantsverdriet, A.F.P. Engelen, A.M. de Jong, W. Wieldraaijer, G.J. Kramer, Appl. Surf. Sci. 144–145 (1999) 366.
[16] S.K. Lim, K.J. Chung, Y.H. Kim, C.K. Kim, C.S. Yoon, J. Colloid Interface Sci. 273 (2004) 517.
[17] T.J. Daou, J.M. Greneche, G. Pourroy, S. Buathong, A. Derory, C. Ulhaq-Bouillet, B. Donnio, D. Guillon, S. Begin-Colin, Chem. Mater. 20 (2008) 5869.
[18] C.C. Berry, A.S.G. Curtis, J. Phys. D: Appl. Phys. 36 (2003) R198.
[19] Q.A. Pankhurst, J. Connolly, S.K. Jones, J. Dobson, J. Phys. D: Appl. Phys. 36 (2003) R167.
[20] S. Mornet, S. Vasseur, F. Grasset, E. Duguet, J. Mater. Chem. 14 (2004) 2161.
[21] A.K. Gupta, M. Gupta, Biomaterials 26 (2005) 3995.
[22] T. Neuberger, B. Schopf, H. Hofmann, M. Hofmann, B. von Rechenberg, J. Magn. Magn. Mater. 293 (2005) 483.
[23] M. Arruebo, R. Fernandez-Pacheco, M.R. Ibarra, J. Santamaria, Nano Today 2 (2007) 22.
[24] R.P. Tandon, M.R. Tripathy, A.K. Arora, S. Hotchandani, Sens. Actuators B 114 (2006) 768.
[25] X.L. Gou, G.X. Wang, X.Y. Kong, D. Wexler, J. Horvat, J. Yang, J. Park, Chem. Eur. J. 14 (2008) 5996.
[26] X.L. Fang, C. Chen, M.S. Jin, Q. Kuang, Z.X. Xie, S.Y. Xie, R.B. Huang, L.S. Zheng, J. Mater. Chem. 19 (2009) 6154.
[27] P. Li, D.E. Miser, S. Rabiei, R.T. Yadav, M.R. Hajaligol, Appl. Catal. B 43 (2003) 151.
[28] S.C. Kwon, M. Fan, T.D. Wheelock, B. Saha, Sep. Purif. Technol. 58 (2007) 40.
[29] H. Jung, H. Park, J. Kim, J.H. Lee, H.G. Hur, N.V. Myung, H. Choi, Environ. Sci. Technol. 41 (2007) 4741.
[30] G.J. Hutchings, M.S. Hall, A.F. Carley, P. Landon, B.E. Solsona, C.J. Kiely, A. Herzing, M. Makkee, J.A. Moulijn, A. Overweg, J.C. Fierro-Gonzalez, J. Guzman, B.C. Gates, J. Catal. 242 (2006) 71.
[31] S.T. Daniells, A.R. Overweg, M. Makkee, J.A. Moulijn, J. Catal. 230 (2005) 52–65.
[32] R.J.H. Grisel, C.J. Weststrate, A. Goossens, M.W.J. Crajé, A.M. van der Kraan, B.E. Nieuwenhuys, Catal. Today 72 (2002) 123.
[33] H.C. Choi, S. Kundaria, D.W. Wang, A. Javey, Q. Wang, M. Rolandi, H.J. Dai, Nano Lett. 3 (2003) 157.
[34] S.J. Han, T.K. Yu, J. Park, B. Koo, J. Joo, T. Hyeon, S. Hong, J. Im, J. Phys. Chem. B 108 (2004) 8091.
[35] M. Ishida, H. Hongo, F. Nihey, Y. Ochiai, Jpn. J. Appl. Phys. 2 43 (2004) L1356.
[36] S. Lastella, Y.J. Jung, H.C. Yang, R. Vajtai, P.M. Ajayan, C.Y. Ryu, D.A. Rider, I. Manners, J. Mater. Chem. 14 (2004) 1791.
[37] J.Y. Raty, F. Gygi, G. Galli, Phys. Rev. Lett. 95 (2005) 096103.
[38] S. Hofmann, R. Sharma, C. Ducati, G. Du, C. Mattevi, C. Cepek, M. Cantoro, S. Pisana, A. Parvez, F. Cervantes-Sodi, A.C. Ferrari, R. Dunin-Borkowski, S. Lizzit, L. Petaccia, A. Goldoni, J. Robertson, Nano Lett. 7 (2007) 602.
[39] J. Park, K.J. An, Y.S. Hwang, J.G. Park, H.J. Noh, J.Y. Kim, J.H. Park, N.M. Hwang, T. Hyeon, Nat. Mater. 3 (2004) 891.
[40] W.W. Yu, J.C. Falkner, C.T. Yavuz, V.L. Colvin, Chem. Commun. (2004) 2306–2307.
[41] X. Liang, X. Wang, J. Zhuang, Y.T. Chen, D.S. Wang, Y.D. Li, Adv. Funct. Mater. 16 (2006) 1805.
[42] J. Park, J. Joo, S.G. Kwon, Y. Jang, T. Hyeon, Angew. Chem. Int. Ed. 46 (2007) 4630.
[43] S.B. Wang, Y.L. Min, S.H. Yu, J. Phys. Chem. C 111 (2007) 3551.
[44] C. Ruby, B. Humbert, J. Fusy, Surf. Interface Anal. 29 (2000) 377.
[45] C.R. Brundle, T.J. Chuang, K. Wandelt, Surf. Sci. 68 (1977) 459.
[46] J.B. Butt, Catal. Lett. 7 (1991) 61.
[47] F. Bonnet, F. Ropital, P. Lecour, D. Espinat, Y. Huiban, L. Gengembre, Y. Berthier, P. Marcus, Surf. Interface Anal. 34 (2002) 418.
[48] R.T. Downs, M. Hall-Wallace, Am. Mineral 88 (2003) 247.
[49] Y.M. Jin, H.F. Xu, A.K. Datye, Microsc. Microanal. 12 (2006) 124.
[50] M.D. Shroff, D.S. Kalakkad, K.E. Coulter, S.D. Kohler, M.S. Harrington, N.B. Jackson, A.G. Sault, A.K. Datye, J. Catal. 156 (1995) 185.
[51] D.B. Bukur, K. Okabe, M.P. Rosynek, C.P. Li, D.J. Wang, K.R.P.M. Rao, G.P. Huffman, J. Catal. 155 (1995) 353.
[52] B.S. Wu, L. Tian, H.W. Xiang, Z.X. Zhang, Y.W. Li, Catal. Lett. 102 (2005) 211.
[53] A.F.H. Wielers, A.J.H.M. Kock, C.E.C.A. Hop, J.W. Geus, A.M. Vanderkraan, J. Catal. 117 (1989) 1.
[54] K.R.P.M. Rao, F.E. Huggins, V. Mahajan, G.P. Huffman, V.U.S. Rao, B.L. Bhatt, D.B. Bukur, B.H. Davis, R.J. Obrien, Top. Catal. 2 (1995) 71.
[55] E. de Smit, A.M. Beale, S. Nikitenko, B.M. Weckhuysen, J. Catal. 262 (2009) 244.